

Article

Hydrodynamic Modelling of Municipal Solid Waste Residues in a Pilot Scale Fluidized Bed Reactor

João Cardoso ¹, Valter Silva ^{1,2,*} , Daniela Eusébio ¹ and Paulo Brito ¹

¹ C3i—Interdisciplinary Center for Research and Innovation, Polytechnic Institute of Portalegre, 7300-110 Portalegre, Portugal; jps.cardoso@ipportalegre.pt (J.C.); danielafle@ipportalegre.pt (D.E.); pbrito@estgp.pt (P.B.)

² INEGI-FEUP, Faculty of Engineering, University of Porto, 4200-465 Porto, Portugal

* Correspondence: valter.silva@ipportalegre.pt; Tel.: +351-245-301-592

Academic Editor: Vasily Novozhilov

Received: 11 September 2017; Accepted: 31 October 2017; Published: 3 November 2017

Abstract: The present study investigates the hydrodynamics and heat transfer behavior of municipal solid waste (MSW) gasification in a pilot scale bubbling fluidized bed reactor. A multiphase 2-D numerical model following an Eulerian-Eulerian approach within the FLUENT framework was implemented. User defined functions (UDFs) were coupled to improve hydrodynamics and heat transfer phenomena, and to minimize deviations between the experimental and numerical results. A grid independence study was accomplished through comparison of the bed volume fraction profiles and by reasoning the grid accuracy and computational cost. The standard deviation concept was used to determine the mixing quality indexes. Simulated results showed that UDFs improvements increased the accuracy of the mathematical model. Smaller size ratio of the MSW-dolomite mixture revealed a more uniform mixing, and larger ratios enhanced segregation. Also, increased superficial gas velocity promoted the solid particles mixing. Heat transfer within the fluidized bed showed strong dependence on the MSW solid particles sizes, with smaller particles revealing a more effective process.

Keywords: hydrodynamics; mixing and segregation; heat transfer; municipal solid waste gasification; pilot scale fluidized bed reactor; CFD FLUENT

1. Introduction

Consumer society habits acquired throughout years of economic growth and urban development have led to an increased volume of produced municipal solid waste (MSW) [1]. In 2015 the worldwide MSW generation was approximately 1300 million tons per year, with predictions dictating an annual growth rate of 4 to 5.6% in developed countries and 2 to 3% in underdeveloped ones [2,3]. By the year of 2025 MSW should amount to an astonishing quantity of 2600 million tons per year, doubling its amount in a mere 10-year period. Such indicators come from assuming a current daily consumption of 1.2 kg of MSW per capita, increasing to an estimated 1.42 kg per capita by the year of 2025 [2].

Regarding the global primary energy demands, fossil fuels still take the lead in energetic dependency with nearly an 86% share by 2016, while nuclear-hydroelectric and renewables have barely an 11% and 3% share, respectively [4]. Given the threats associated with the reliance on quickly depleting fossil fuels and the severe environmental issues related to the greenhouse gas emissions that accrue, it is therefore time to rethink energy policies [5]. For instance, major companies such as Volvo took a stand towards reducing the carbon footprint, committing to pull the plug on gas fueled engines and replace them with fully electric or hybrid technology from 2019 onwards [6]. Thus, a set of changes to reduce the consumption of non-renewables aiming at better energy infrastructure and climate change prospects have been observed.

Waste-to-energy (WtE) conversion methods offer an alluring solution not only to the ongoing energy problem, but also in waste disposal, by reducing the volume of landfilled waste and increasing the recycling rates [7]. Here, MSW can be an important part of the equation as a huge and perpetual energy source due to its endless abundance generated by populations on a daily basis. Waste incineration was initially introduced as a potential solution, however, the high associated costs, tight air pollution regulations and ash disposal challenges made room for more viable alternatives [8]. Gasification is a thermo-chemical process that converts carbon-based feedstocks into a highly energetic and combustible gas mixture known as syngas [9]. Recent reports not only indicate waste gasification as feasible, but also capable of treating MSW with fewer emissions than other treatment methods [10,11]. Such assertions have made gasification a rather attractive WtE method from an economic and energetic point of view, meeting the World's current growing demands for a more efficient and cleaner energy.

Niu et al. [12] developed a comprehensive process model to simulate the thermodynamic performance of MSW gasification in a bubbling fluidized bed reactor. The authors varied an operating parameter, namely the gasification temperature, and analyzed the effect on the reactor efficiency and syngas composition. Results showed that increased temperatures, no higher than 900 °C, favored the gasification efficiency by improving the performance and combustibility of the syngas.

Begum et al. [13] corroborated the results of Niu and colleagues [12] regarding the gasification temperature effect on gasification performance, and improved the approach by implementing a model validation process by comparison with experimental data retrieved from the literature, further extending the gasification model to other biomass related feedstocks.

Effects of MSW particle size at different operating temperatures and their direct influence on the syngas yield and composition were studied by Luo et al. [14]. Gasification runs showed that smaller particles resulted in improved gas efficiency, and higher temperatures enhanced the syngas yield, reducing the char and tar appearance.

Reactor hydrodynamics with respect to waste gasification are seldom mentioned, regardless of their crucial importance, as it strongly influences all the fundamental properties within the gasification system. On this subject, Arena et al. [15] discussed the key role of hydrodynamics and how it strongly affects the quality of the fluidization, by highlighting its dominance in all physical and chemical processes occurring during the gasification process. Heat transfer, gas and solids mixing, temperature distribution, residence time, and particles size and density are some of the main features dealt.

Couto et al. [16] assessed the potential of Portuguese MSW by applying an extensively validated numerical model to the steam gasification approach. The authors evaluated the results by comparison with data previously obtained for Portuguese biomass feedstock gasification. Numerical and experimental results were found to be in good agreement. The conclusions showed that MSW syngas presented inferior yields when compared to biomass products. Nonetheless, the study presented the economic benefits regarding the current municipal waste logistic infrastructure, currently inexistent for biomass resources, enhancing the resourceful characteristics of MSW as an easily accessible feedstock.

The research group succeeded in demonstrating, through several published works, the constant ongoing evolution of the mathematical model, starting its first application on biomass substrates [17,18], followed the inclusion of various gasification agents and the upgrade to deal with the intrinsic heterogeneity of MSW [16,19–21]. Here, within the developed mathematical model, complex phenomena like hydrodynamics were included and considered, however the authors did not provide a deep analysis concerning this particular subject.

There are, to the best of our knowledge, limited studies on CFD simulation concerning the hydrodynamics of MSW gasification in pilot scale fluidized bed reactors. This analysis focuses in presenting useful data on this matter and emphasizes the promising usage of MSW in gasification. Thereby, the main purpose of this work is to present a 2-D multiphase model dealing with MSW gasification, using an Eulerian-Eulerian approach within the ANSYS FLUENT framework, coupled with UDFs applied to improve the reactor hydrodynamic behavior. The mathematical model validation was assessed by comparison to experimental results. A grid resolution analysis

was developed in order to reach a proper solution respecting its certainty and computational cost. Hydrodynamics within the fluidized bed was modeled with special care, taking detail on solids mixing/segregation phenomena and heat transfer, herewith relating different operating variables and bed conditions.

2. MSW: A Portuguese Case Scenario

Portugal has made considerable progress in what comes to waste management performance. By the end of the last century Portugal still used dump disposal as the dominant treatment method [22]. Implementation of waste management measures led to a trendy landfill disposal reduction over the years, setting up goals for waste reuse, recycling and recovery. With various measures applied over the last twenty years Portugal has managed to increase the proportion of waste selectively collected from 1.1% to 13.6% [23]. Figure 1 places Portugal in the European Union scenario, accounting the total amount of waste generated (kg per capita) together with other 27 European countries, in the years 2010 and 2015. Statistics show that the MSW produced varied from 789 kg per capita in Denmark, to 247 kg per capita in Romania, with Portugal accounting 452 kg per capita. These variations are related not only with consumer habits and economic wealth, as richer countries tend to show increased consumption demands, but also with waste treatment and disposal measures lying within each member state [24]. From 2010 to 2015, Portugal and other 14 out of 28 countries cut back their waste production, with Bulgaria showing the largest reduction with an annual average decrease of 2.5% [24]. Also, 15 of the 28 nations showed, in 2015, a waste generation rate sitting below the European average, Portugal included.

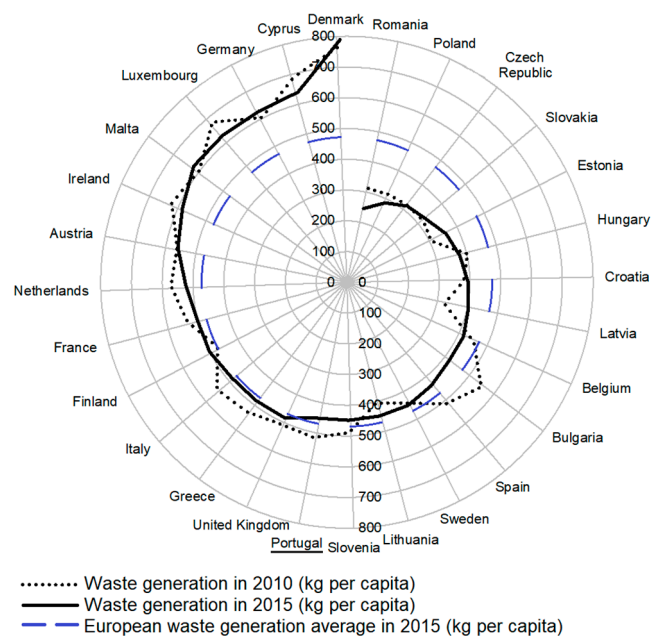


Figure 1. MSW generated per person in 28 European countries (2010 and 2015).

Current distribution regarding the Portuguese waste treatment management is depicted in Figure 2. MSW produced in Portugal during 2016 was still mainly direct towards landfill disposal (29%), followed by mechanical and biological treatment (27%), energy recovery (22%), mechanical treatment (10%), recycling (10%), and composting (2%). In 2016, the total amount of MSW sent to landfills dropped, confirming the reduction trends and allowing a decrease of 41% compared to numbers recorded in 1995 [25]. The introduction of new treatment and recovery facilities allowed for a direct landfill disposal reduction and an amount increase on recovered recyclable waste [25]. However, from 2015 to 2016 a slight increase of 3% on the total amount of waste generated was

detected, which may hamper the achievement of the defined goals for 2020, integrated in the National Waste Management Plans (PERSU 2020). PERSU 2020 holds as main concerns: 50% waste recycling increase by phasing out direct landfill up to 35% until 2020; support the efficiency increase of MSW management systems and infrastructures; and setting a minimum of 45 kg per capita of waste selectively collected [23]. The achievement of these committed targets is now dependent on the optimization of the existing mechanical and biological waste treatment units, and in a social responsibility pointing towards ecological habits [26].

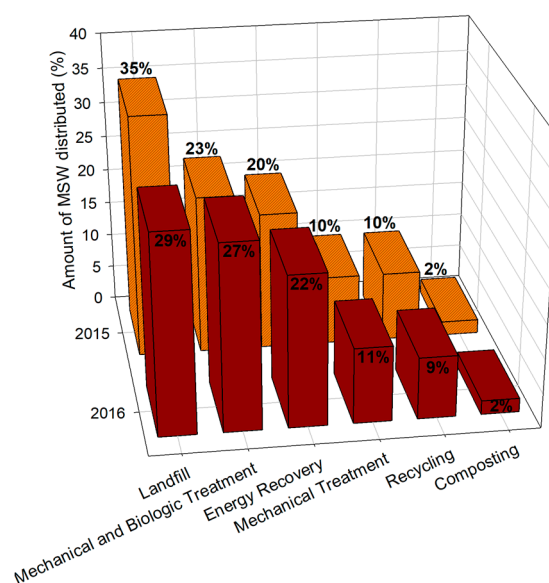


Figure 2. Portuguese MSW distributed by treatment type (2015 and 2016).

Implementation of WtE methods offers a helping hand in achieving the 2020 targets. Thermo-chemical waste conversion technologies include incineration, pyrolysis and gasification. Gasification and pyrolysis make use of a controlled environment to convert waste into valuable commercial products such as syngas, a by-product that once purified can be used as a feedstock for petro-chemicals and other applications [27], whereas incineration simply burns waste to create heat and produce electricity. Also, negative environmental impacts are frequently associated to this method, making incineration into a less feasible WtE process [27]. Thus, gasification and pyrolysis deliver better prospects in waste recovering than incineration [27]. Gasification in particular takes a further step within the thermal decomposition processes, being very cost competitive in comparison with incineration, aside from offering better environmental performance [28]. Portugal relies mostly on incineration as the primary thermo-chemical energy recovery method, while other European countries such as Sweden, Denmark and the Netherlands already have high contributions from waste gasification [29]. In an economic point of view, by turning waste into a resourceful feedstock gasification applied to MSW conversion can reduce the municipal waste management costs and provide a source of income [27]. In this manner, gasification appears as an increasingly attractive and clean solution to treat MSW, becoming a valuable option to achieve the established environmental goals.

Waste composition analysis is an important step to evaluate the potential for valorization [26]. MSW physical composition in mainland Portugal by the year of 2015 is presented in Figure 3. In this study, the MSW used [16] was collected from Northern Portugal. Table 1 shows the average physical characteristics of the MSW considered. Both waste samples agree specially in the main compositors, putrefied residues, paper/cardboard, textiles, fine elements, plastics and glass. Remaining composition differences seen are due to the fact that MSW physical composition is strongly dependent on the collection region and season, as they tend to vary with the consumption habits [26].

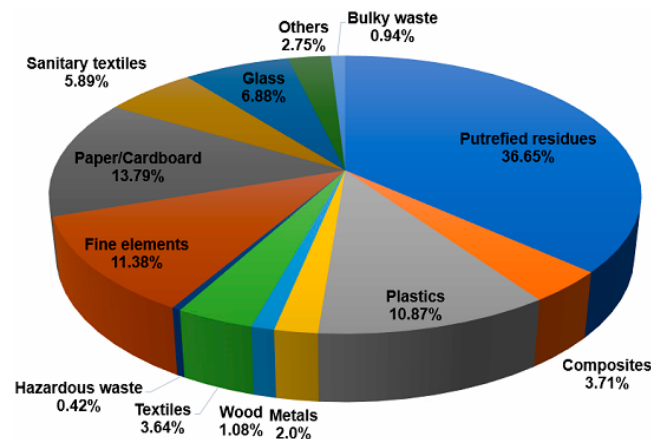


Figure 3. Average physical characterization of MSW produced in Portugal in 2015.

Table 1. Physical characterization of the MSW used in this study [16].

Physical Characterization	MSW (wt %)
Putrefied residues	38
Paper/Cardboard	10
Composites	6
Textiles	8
Sanitary textiles	9
Plastics	12
Glass	6
Metals	3
Fine elements	8

3. Experimental Settings

3.1. Pilot Scale Fluidized Bed Reactor Setup

The main specifications of the gasification plant are presented in Figure 4. The unit, located at the Polytechnic Institute of Portalegre (Portugal), includes a feeding system that drops the substrate into the reactor at a height of 0.4 m from the base, being the feeding speed controlled by means of an Archimedes' screw. The 250 kW_{th} fluidized bed reactor is 0.5 m wide and 4.15 m height, with a static bed height of 0.15 m composed of 70 kg of dolomite (calcium magnesium carbonate CaMg(CO₃)₂). The reactor operates under atmospheric pressure with a maximum feedstock rate of 70 kg/h and at the bottom of the reactor a set of diffusers deliver an approximate flow of 70 m³/h of preheated air. There is a gas-cooling system composed by two heat exchangers cool the syngas to about 570 K and 420 K, respectively. The black carbon and ash particles produced during the gasification process are collected into a bag and a condenser is used to withdraw the liquids from the syngas by cooling it to room temperature in a tube heat exchanger.

Syngas analysis is performed in a 450-GC gas chromatograph (Varian, Palo Alto, CA, USA) equipped with two TCD detectors that allow the detection of H₂, CO, CO₂, CH₄, O₂, N₂, C₂H₆, C₂H₄ (equipped respectively with CP81069, CP81071, CP81072, CP81073 and CP81025 Varian GC columns), using helium and nitrogen as carrier gases. Syngas samples are collected in appropriate collection and analysis Tedlar bags at the condenser exit every time gasification of a given feedstock composition has reached its stationary state. Collected syngas samples are injected directly from the sampling bags in the chromatograph (within one hour after sampling) using a peristaltic pump operating at its maximum rate through a Marpren tube. Chromatographic peaks for the different gases under analysis are identified based on their retention times, and by comparing them with the retention times of the same gases in the reference chromatogram of the custom solution, provided by

Varian. Gas mass percentage composition is calculated on the basis of peak areas under the chromatographic signals.

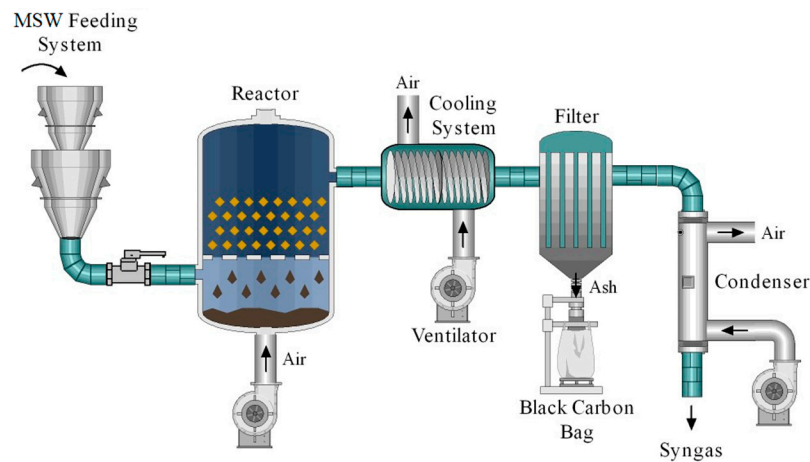


Figure 4. Schematics concerning the main components of the pilot scale gasification plant at the Polytechnic Institute of Portalegre, Portugal.

3.2. Computational Setup

A computational geometry domain designed with a width of 0.50 m and height 4.15 m was set up to closely mimic the experimental conditions established for the fluidized bed reactor. Bed height was set to 0.15 m, atmospheric air was delivered at the bottom of the reactor (inlet) and the resulting syngas leaves through an opening located at the top right corner of the geometry (outlet). The transient model was set with a time step size of 10^{-4} s, for a total simulation time of 50 s (50,000 time steps). For convenience sake, most results are shown at a simulation time of 3 s, given that at this interval the fluidized bed trends were already noticeable. Table 2 details the remaining simulations parameters.

Table 2. Bed configurations and simulation parameters [16,30–32].

Dolomite density (kg/m^3)	2870
Dolomite diameter (m)	0.0005
MSW density (kg/m^3)	247
MSW diameters (m)	0.002, 0.005, 0.008
Superficial gas velocities (m/s)	0.15, 0.25, 0.40
Operating temperatures (K)	873, 973, 1073
Initial volume fraction	0.60
Maximum packing limit	0.63
Drag model	modified Syamlal-O'Brien (UDFs configured)
Heat interaction (solid-air/solid-solid)	Gunn/Tomyama
Specific heat ($\text{J}/\text{kg}\cdot\text{K}$)	UDFs configured
Thermal conductivity ($\text{W}/\text{m}\cdot\text{K}$)	UDFs configured
Granular bulk viscosity ($\text{Kg}/\text{m}\cdot\text{s}$)	Lun-et al.

4. Mathematical Model

MSW gasification is a rather complex process to interpret given the substantial number of physical and chemical interactions taking place. Such complex process was studied by implementing a two-dimensional multiphase model within the FLUENT database. Our model was firstly developed in the study of biomass gasification by Silva et al. [17,19], being later extended to MSW gasification [20,21,33]. The model considers the gas phase as continuous, and the two solid phases (dolomite and MSW) follow an Eulerian granular model. Both gas and solid phases are defined through a set of conservation

equations for mass, momentum and energy. In this study, the hydrodynamic behavior within the fluidized bed reactor earned special attention. The hydrodynamics and heat transfer phenomena within the fluidized bed were enhanced by including user defined functions (UDFs). Syngas composition was then studied for validation purposes.

4.1. Mass Balance Model

The gas (g) and solid (s) phases continuity equations are:

$$\frac{\partial}{\partial t}(\alpha_g \rho_g) + \nabla \cdot (\alpha_g \rho_g \vec{v}_g) = S_{gs} \quad (1)$$

$$\frac{\partial}{\partial t}(\alpha_s \rho_s) + \nabla \cdot (\alpha_s \rho_s \vec{v}_s) = S_{sg} \quad (2)$$

where α , ρ , and \vec{v} , are the volume fraction, bulk density, and velocity, of gas and solid phases, respectively. Mass exchange occurs between the phases, defining the mass source term (S) which is given by:

$$S_{gs} = -S_{sg} = M_c \sum \gamma_c R_c \quad (3)$$

Concerning the phase density, solid phase was considered as constant. As for the gas phase density the ideal gas behavior goes as follow:

$$\frac{1}{\rho_g} = \frac{RT}{p} \sum_{i=1}^n \frac{Y_i}{M_i} \quad (4)$$

4.2. Momentum Equations

The gas phase momentum equation is presented as:

$$\frac{\partial}{\partial t}(\alpha_g \rho_g \vec{v}_g) + \nabla \cdot (\alpha_g \rho_g \vec{v}_g \vec{v}_g) = -\alpha_g \cdot \nabla p_g + \nabla \cdot \alpha_g \bar{\tau}_g + \alpha_g \rho_g \vec{g} + \beta(\vec{v}_g - \vec{v}_s) + S_{gs} U_s \quad (5)$$

where $\bar{\tau}_g$ is the stress tensor for the gas phase, \vec{g} is the gravitational acceleration, β is the gas-solid interaction drag force, S_{gs} is the source term of the gas-solid interphase, and U_s the solid phase mean velocity.

The solid phases (dolomite and MSW) momentum balance equations are defined as:

$$\begin{aligned} \frac{\partial}{\partial t}(\alpha_{dolomite} \rho_{dolomite} \vec{v}_{dolomite}) + \nabla \cdot (\alpha_{dolomite} \rho_{dolomite} \vec{v}_{dolomite} \vec{v}_{dolomite}) = \\ -\alpha_{dolomite} \cdot \nabla p - \nabla p_{dolomite} + \nabla \cdot \alpha_{dolomite} \bar{\tau}_{dolomite} + \alpha_{dolomite} \rho_{dolomite} \vec{g} + \\ \beta_{g/dolomite}(\vec{v}_g - \vec{v}_{dolomite}) + \beta_{dolomite/msw}(\vec{v}_{dolomite} - \vec{v}_{msw}) + S_{dolomite/g} U_{dolomite} \end{aligned} \quad (6)$$

$$\begin{aligned} \frac{\partial}{\partial t}(\alpha_{msw} \rho_{msw} \vec{v}_{msw}) + \nabla \cdot (\alpha_{msw} \rho_{msw} \vec{v}_{msw} \vec{v}_{msw}) = \\ -\alpha_{msw} \cdot \nabla p - \nabla p_{msw} + \nabla \cdot \alpha_{msw} \bar{\tau}_{msw} + \alpha_{msw} \rho_{msw} \vec{g} + \\ \beta_{g/msw}(\vec{v}_g - \vec{v}_{msw}) + \beta_{msw/dolomite}(\vec{v}_{msw} - \vec{v}_{dolomite}) + S_{msw/g} U_{msw} \end{aligned} \quad (7)$$

The dolomite phase is given by Equation (6), and the MSW phase is presented by Equation (7). Here, $\bar{\tau}$ is the MSW phase stress tensor and p is the solid phase pressure. The terms $\beta_{g/dolomite}$ and $\beta_{g/msw}$ give out the gas-dolomite and gas-MSW interaction drag force coefficient; $\beta_{dolomite/msw}$ and $\beta_{msw/dolomite}$ present the dolomite-MSW interaction drag force coefficient and vice-versa.

4.3. Energy Conservation Equation

Here the default gas and solid phases heat absorption and transfer coefficient were enhanced by applying a polynomial routine UDFs.

The energy conservation equation for both gas phase and solid phases can be defined as:

$$\frac{\partial}{\partial t} (\alpha_q \rho_q \vec{v}_q) + \nabla \cdot (\alpha_q \rho_q \vec{v}_q h_q) = \alpha_q \frac{\partial}{\partial t} (p_q) + \bar{\tau}_q : \nabla \cdot \vec{v}_q - \nabla \cdot \vec{q}_q + S_q + \sum_{p=1}^n (\vec{Q}_{pq} + \dot{m}_{pq} h_{pq} - \dot{m}_{qp} h_{qp}) \quad (8)$$

The term \vec{Q}_{pq} is the heat exchange between gas and solid phases, h_q the specific enthalpy of phase q th, \vec{q}_q the conductive heat flux, S_q the source term, and h_{pq} the enthalpy of the interphase. The heat transfer coefficient between the gas and solid phases is expressed as follows:

$$\vec{Q}_{pq} = h_{pq} (T_p - T_q) \quad (9)$$

The convective heat transfer coefficient is determined by the Nusselt number, k_p specifies the thermal conductivity for phase p th:

$$h_{pq} = \frac{6k_p \alpha_q \alpha_p Nu_q}{d_p^2} \quad (10)$$

The Nusselt number is presented by:

$$Nu_s = \frac{h_{gs} d_s}{k_g} = (7 - 10\alpha_g + 5\alpha_g^2) \left(1 + 0.7 Re_s^{0.2} Pr_g^{0.33}\right) + (1.33 - 2.4\alpha_g + 1.2\alpha_g^2) Re_s^{0.7} Pr_g^{0.33} \quad (11)$$

where Re_s is the Reynolds number and Pr_g the gas phase Prandtl number.

4.4. Granular Eulerian Model

The kinetic energy of the random particles motion is given by the granular temperature, described by the following conservation equation for the kinetic theory of gases:

$$\frac{3}{2} \left[\left(\frac{\partial (\rho_s \alpha_s \Theta_s)}{\partial t} + \nabla \cdot (\rho_s \alpha_s \vec{v}_s \Theta_s) \right) \right] = (-P_s \bar{I} + \bar{\tau}_s) : \nabla (\vec{v}_s) + \nabla (k_{\theta_s} \nabla \Theta_s) - \gamma_{\theta_s} + \varphi_{gs} \quad (12)$$

where the term γ_{θ_s} is the collisional dissipation of energy, \vec{v}_s the diffusive flux of granular energy, φ_{gs} the granular energy exchange between the gas and solid phases, and k_{θ_s} the diffusion coefficient.

The diffusion coefficient may be written as follows [34]:

$$k_{\theta_s} = 15d_s/4(41 - 33\omega)\rho_s\alpha_s\sqrt{\theta_s\pi} \cdot \left[1 + \frac{12}{5}\omega^2(4\omega - 3)\alpha_s g_{o,ss} + \frac{16}{15\pi}(41 - 33\omega)\omega\alpha_s g_{o,ss} \right] \quad (13)$$

where $\omega = 1/2(1 + e_{ss})$.

The solids pressure relates the kinetic term and the particle collisions term, expression derived from Lun et al. [35]:

$$p_s = \alpha_s \rho_s \theta_s + 2\rho_s(1 + e_{ss})\alpha_s^2 g_{o,ss} \theta_s \quad (14)$$

where e_{ss} is the restitution coefficient and $g_{o,ss}$ is the radial distribution function.

4.5. Drag Model

In this modeling approach, the interaction between gas and solid phases is accomplished by the drag force. The default Syamlal-O'Brien drag law was customized by means of a UDFs applied to better predict the fluidized bed hydrodynamics.

Syamlal-O'Brien drag function for a single spherical particle is given below:

$$K_{gs} = \frac{3}{4} \frac{\alpha_s \alpha_g \rho_g}{v_{r,s}^2 d_s} C_D \left(\frac{Re_s}{v_{r,s}} \right) \left| \vec{v}_s - \vec{v}_g \right| \quad (15)$$

where K_{gs} is the gas-solid momentum transfer coefficient, $v_{r,s}$ is the terminal velocity coefficient for the solid phase, Re is the Reynolds number, d_s solid particles diameter and C_D the drag coefficient, which can be written as:

$$C_D = \left(0.63 + \frac{4.8}{\sqrt{Re_s/v_{r,s}}} \right)^2 \quad (16)$$

4.6. Chemical Reactions Model

In this work, the hydrodynamics sub-model is of main concern to capture, nevertheless an overview concerning the main chemical reactions considered is provided in Table 3. Additional data concerning the model can be found somewhere else [17–19]. Proximate and elementary analysis of the MSW fuel utilized is presented in Table 4.

Table 3. Chemical reactions model.

Reactions	Arrhenius Reactions Rate
MSW Pyrolysis:	
Cellulose $\xrightarrow{r_1}$ $\alpha_1 volatiles + \alpha_2 TAR + \alpha_3 char$	$r_1 = A_i \exp\left(\frac{-E_i}{T_s}\right) (1 - a_i)^n$
Hemicellulose $\xrightarrow{r_2}$ $\alpha_4 volatiles + \alpha_5 TAR + \alpha_6 char$	$r_2 = A_i \exp\left(\frac{-E_i}{T_s}\right) (1 - a_i)^n$
Lignin $\xrightarrow{r_3}$ $\alpha_7 volatiles + \alpha_8 TAR + \alpha_9 char$	$r_3 = A_i \exp\left(\frac{-E_i}{T_s}\right) (1 - a_i)^n$
Plastics $\xrightarrow{r_4}$ $\alpha_{10} volatiles + \alpha_{11} TAR + \alpha_{12} char$	$r_4 = \left[\sum_{i=1}^n A_i \exp\left(\frac{-E_i}{RT}\right) \right] \rho_v$
PrimaryTAR $\xrightarrow{r_5}$ $volatiles + SecondaryTAR$	$r_5 = 9.55 \times 10^4 \exp\left(\frac{-1.12 \times 10^4}{T_s}\right) \rho_{TAR1}$
Homogeneous reactions:	
$CO + H_2O \leftrightarrow CO_2 + H_2$	$r_6 = 5.159 \times 10^{15} \exp\left(\frac{-3430}{T}\right) T^{-1.5} C_{O_2} C_{H_2}^{1.5}$
$C_2H_4 + 2H_2O \leftrightarrow 2CO_2 + 4H_2$	$r_7 = 3100.5 \exp\left(\frac{-15,000}{T}\right) C_{C_2H_4} C_{H_2O}^2$
$CH_4 + H_2O \leftrightarrow CO + 3H_2$	$r_8 = 3.1005 \exp\left(\frac{-15,000}{T}\right) \left[C_{H_2O} C_{CH_4} - \frac{C_{CO} C_{H_2}^3}{0.0265 \left(\frac{32,900}{T}\right)} \right]$
Heterogeneous reactions:	
$C + CO_2 \rightarrow 2CO$	$r_9 = 2082.7 \exp\left(\frac{-18036}{T}\right)$
$C + H_2O \rightarrow CO + H_2$	$r_{10} = 63.3 \exp\left(\frac{-14051}{T}\right)$
Diffusion rate coefficient	Final reaction rate
$D_0 = C_1 [(T_p + T_\infty) \div 2]^{0.75} \div (dp)$	$\frac{d_{mp}}{dt} = -A_p \frac{\rho RT_\infty Z_{0X}}{M_{w,0X}} \frac{D_0 r_{Arrhenius}}{D_0 + r_{Arrhenius}}$

Table 4. Proximal and elemental analysis of the MSW used [16].

Proximal Analysis	MSW (wt %)
Moisture	17.55
Ash	14.92
Volatile matter	76.62
Fixed carbon	8.46
Elemental Analysis	MSW (% , Dry Basis)
C	47.99
H	6.3
N	1.39
O	43.58

4.7. Mixing and Segregation Model

The level of segregation was determined by applying a standard deviation concept given by [36]:

$$S^2 = \frac{1}{(N-1)} \sum_{i=1}^N (y_i - \bar{y})^2 \quad (17)$$

where the terms N , y_i and \bar{y} refer to the number of samples, volume fraction and mean volume fraction, respectively. The segregation index (S) extents from zero, when perfectly mixed, to one, if fully segregated. In opposition, the mixing index ($M = 1 - S$) takes the value of one, when completely mixed, or zero when totally segregated.

4.8. Grid Resolution Analysis

In order to assure a grid independent solution, four different two-dimensional grids with increasing grid density were studied in the present work. Grids were composed of square cells uniformly spaced, with each cell obeying to a maximum size criterion of 10 to 12 times the particle size [37]. Cell size and density for each grid can be seen in Table 5.

Table 5. Grid density parameters.

Grid	Cell Size (mm ²)	No. of Elements
1	10	20,750
2	6.9	40,248
3	4.8	80,808
4	3.4	160,017

Figure 5 compares the instantaneous volume fraction contours for each grid. Simulations for this study were kept at a superficial gas velocity of 0.25 m/s, simulation time of 3 s and operating temperature of 873 K. Volume fraction instantaneous contours show the need of performing a grid independent solution, proving that, by increasing the grid density, solids distribution and bubble formation becomes clearer. Coarser grids (20,750 and 40,248) were incapable of reproducing a proper void fraction (dark blue colored), still denoting the presence of solid material, as displayed in Figure 5. Finer grids on the other hand (80,808 and 160,017), show clearer solid presence (bright red colored) and bubble definition, illustrating less color blurriness along the border areas between the two phases (Figure 5). While finer grids can distinguish solids presence from gas presence more clearly, the coarser grids are inefficient in perceiving the reactor hydrodynamics clearly. With no surprise, results show that finer grids do come closer considering its aspect ratio, while the coarser grid pair deviates considerably. Furthermore, results showed direct dependency on the grid quality, highlighting the importance in considering a grid density analysis, since its absence would have led to incorrect assumptions. Undoubtedly, a finer grid provides more accurate results, yet a balance must be made considering the coarseness of the grid and the computational cost required. The finer grid consumed about 60% more time than the previous with 80,808 elements. Thus, the third grid, besides revealing good agreement with the results obtained from the 160,017 elements, was capable of mimicking the trends shown by the fourth grid, as seen in Figure 5. Therefore, from the considerations retrieved from this analysis it was determined that the 80,808 elements grid was the most appropriate to use, serving in better extent the scope of this work.

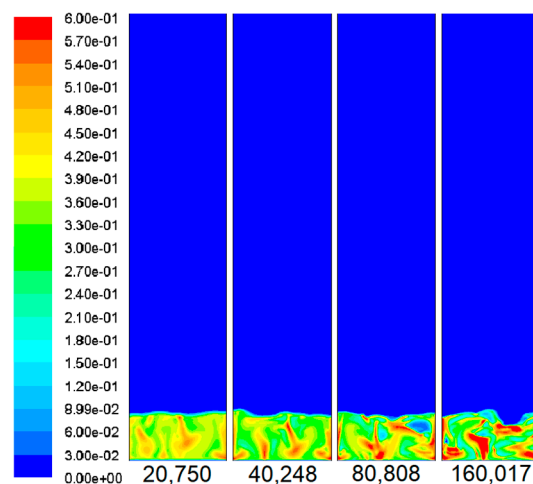


Figure 5. Instantaneous volume fraction contours for the simulation time of 3 s for each of the studied grids.

5. Results and Discussion

5.1. Model Validation

A validation process must be assessed in order to ensure that the right predictions are being made by the previously described mathematical model. For that purpose, a series of considerations must be endorsed. The mathematical model was already extensively validated for biomass substrates, concerning their syngas compositions, by means of experimental gasification runs in the previously described 250 kW_{th} pilot scale fluidized bed reactor [17,18]. In order to minimize deviations between experimental and numerical data, UDFs were included to improve the reactor hydrodynamics and corresponding validation was accomplished with fluidization curves gathered from experimental gasification runs from a 75 kW_{th} pilot scale fluidized bed reactor. These routines implement a set of polynomial equations designed to enhance the standard drag model and heat transfer phenomena features within the applied mathematical model. The drag model and heat transfer adjustments are fulfilled by optimizing the default drag coefficients and gas-solid thermal conductivity parameters within their governing equations, allowing customizing these general correlations to fit our particular modeling needs and to better agree with the experimental setup, regarding boundary conditions and material properties. Thus, the tuned routines provide a more accurate and predictable fitting procedure able to generate a more realistic behavior in different scaled reactors. Figure 6 shows the deviation between the experimental and the numerical fluidization curves retrieved at two different bed heights (8 and 18 cm). Experimental and numerical results without UDFs inclusion are also depicted for the 8 and 18 cm curves. Results made clear that without the use of UDFs routines, the fluidization curves show higher deviations from the experimental results. Once the improvements were established, deviations were within good acceptance and the model was capable of predicting the curves slope behavior with good agreement, turning the fluidization process much more perceptible and closer to a more righteous scenario. A similar strategy was successfully applied to biomass gasification in the 250 kW_{th} reactor, again the experimental and the numerical presented inferior deviations once the UDFs routines were implemented. Indeed, a better agreement between experimental and numerical results for the syngas composition was found with a 15–30% range error deviation decrease for species composition regarding former validations using biomass and MSW [17,20].

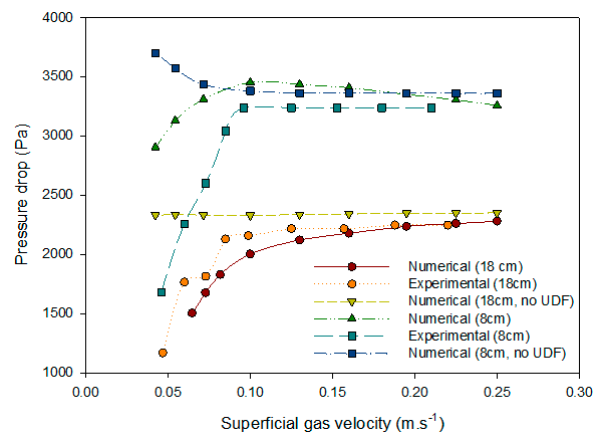


Figure 6. Experimental and numerical pressure drop curves comparison for the 75 kW_{th} reactor measured at 8 cm height and at 18 cm height from the distributor plate.

One occurrence to note is that, regarding the hydrodynamics alone, when no chemical reactions are being considered, biomass and MSW substrates physical characteristics come close, with most of interactions within the fluidized bed being conserved. Critical differences are mainly related with heat exchange because MSW has a high moisture content. To take into account such differences and to evaluate the adequacy of the developed hydrodynamics model, the chemical reactions are included and further validation was accomplished with syngas runs.

5.2. Time-Mean Volume Fraction and Solid Particles Velocity Profiles

The mathematical model once validated, MSW and dolomite simulation runs were accomplished by handling the solids within the simulation setup. Mean volume fraction profiles compared together with the velocity vectors, give an insightful view of the reactor's hydrodynamics by depicting the solids distribution and movement within the fluidized bed. MSW and dolomite interplay was implemented by means of a UDFs concerning drag and heat transfer. Figure 7 presents the pair comparison between MSW and dolomite mean volume fraction contours and the velocity vector profiles at three different superficial gas velocities 0.15, 0.25 and 0.40 m/s, at the simulation time of 3 s. Dolomite, as the inert bed material, is present in a considerably larger amount, while MSW is present in smaller quantities, like in a real gasification process where only a small amount of MSW is continuously fed into the reactor. Solids occupy distinct regions within the bed, dolomite gathers at the bottom of the reactor (the heaviest), and MSW migrates to the bed top due to the up-flow gas (the lightest). Solid particles motion within the fluidized bed is induced by the gas bubbles flow, as the superficial gas velocity increases, bubbles size enlarges, carrying more solid particles within, causing the bed height to increase [38]. Additionally, the inlet gas velocity increase will promote the mixing between the solids species involved [31]. The gas velocity effect over mixing is considered in the next sub section. This bed expansion and particles velocity increase is rather pronounced from 0.15 to 0.40 m/s. MSW and dolomite vector velocity profiles depict a clear particles velocity and turbulence increase, showing vigorous solids movements. Yellow and red colored vectors become more intense and cover larger bed regions as the inlet velocity comes increased. MSW shows no velocity vectors presence near the bed bottom, emphasizing the MSW tendentious presence at higher bed regions. However, higher velocities were measured at the upper and middle bed regions, as solid particles are allowed to move more freely at higher regions, than at lower regions where entrapment may occur [38]. The velocity vectors and the solids distribution along the bed height are in good agreement to the literature [38].

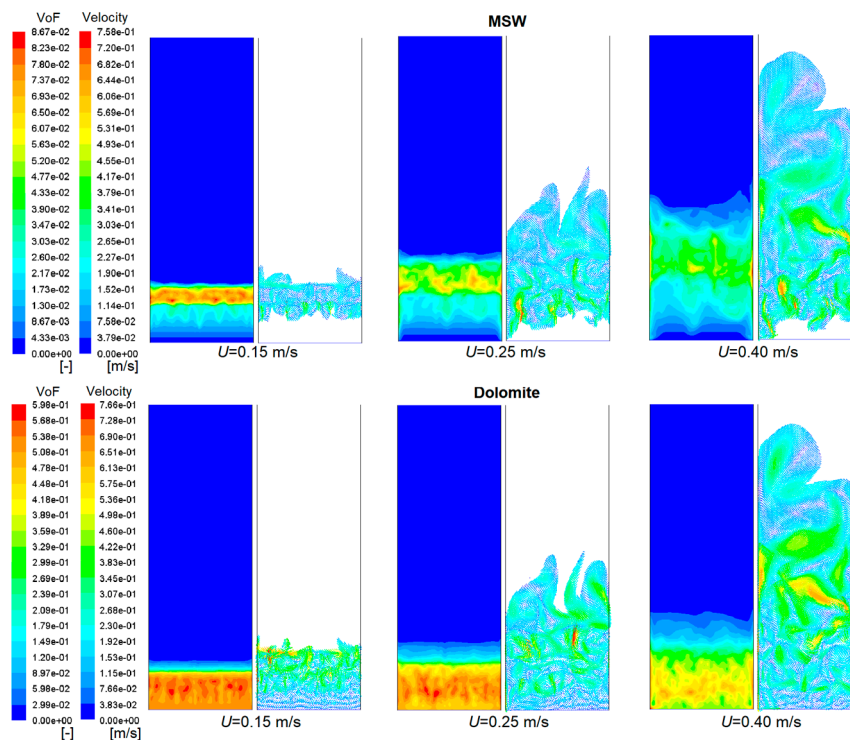


Figure 7. Pairs of time-mean solids volume fractions distributions (left) compared alongside with instantaneous solids velocity vector distributions (right) at three different superficial gas velocities (0.15, 0.25 and 0.40 m/s). MSW particle size 5 mm, operating temperature 873 K and simulation time 3 s.

The simulated time-mean axial (or lateral) MSW and dolomite particles velocity at three different superficial gas velocities (0.15, 0.25 and 0.40 m/s), gathered at two distinct bed heights (8 and 16 cm) are shown in Figure 8a–d. Lateral velocity results showed that MSW particles revealed a generalized increased axial velocity at both bed heights, particularly in the center bed regions, when compared to dolomite particles. MSW due to being the lighter component showed increased axial velocity, while the heavier dolomite revealed inferior axial movement [39]. However, a high reaching peak can be seen for both dolomite profiles (8 and 16 cm) in the right near wall region about 0.50 m (Figure 8b,d). Such an effect may be due to a lateral acceleration induced by bubbles over the dolomite particles towards the wall region [39]. Indeed, as the inlet velocity is increased, higher axial velocity is measured in the near wall regions. The gas flow increase within the fluidized bed will confer more kinetic energy into the solid particles, increasing the turbulence effect, and in turn, the lateral solids dispersion, which may be compelling the solid particles to move towards the reactor's walls increasing the axial near wall velocity [39]. Concerning the bed height, the profiles showed a higher particle velocity at 16 cm height than at 8 cm height. Similar conclusions were reached from the velocity vectors regarding the solids increased velocities in higher bed regions, due to more interparticle space and freedom to move, and also higher bubble rise and collapse movements [38]. Moreover, the axial particle velocities were found to increase with the superficial gas velocity, which is consistent with previous observations from the velocity vector profiles. The higher the superficial gas velocity is, the higher the drag force exerted upon the solid particles will be, leading to an increased particles velocity. However, some peaks from the 0.25 m/s profile are seen to surpass the 0.40 m/s profile, this may be given to the particles collisions and chaotic flow induced by greater velocities, casting solid particles into lateral opposing directions resulting in reduced axial velocity [39].

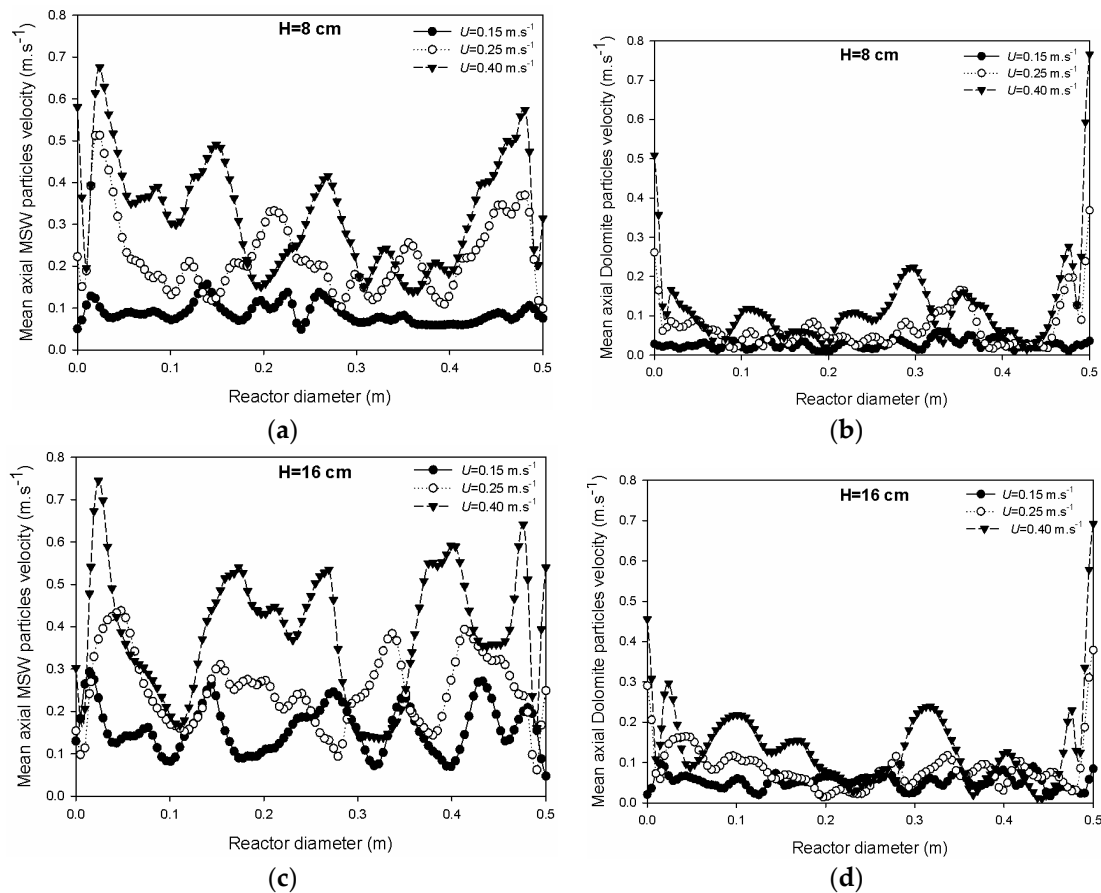


Figure 8. Solid particles time-mean axial velocity profiles at three different superficial gas velocities (0.15, 0.25, 0.4 m/s): (a) MSW velocity at 8 cm height; (b) dolomite velocity at 8 cm height; (c) MSW velocity at 16 cm height; (d) dolomite velocity at 16 cm height. MSW particle size 5 mm, dolomite particle size 0.5 mm, operating temperature 873 K and simulation time 3 s.

5.3. Mixing and Segregation Phenomena

When a binary mixture is submitted to a fluidization process, the solid particles enclosed tend to separate or join accordingly to their individual physical characteristics, either being their size or density. Segregation occurs when the particles size or density ratio is larger. Mixing on the other hand, is the opposite effect of segregation, occurring when the particles size or density ratio is lower. Mixing and segregation phenomena retain crucial importance for both industrial applications and theoretical studies. Good mixing is generally required in gas-solid contact reactors, while segregation is usually desirable for applications in which solids should be separated according to their size or density. In fluidized bed studies segregation weakens the fluidization performance by creating an unbalanced solids distribution.

In this work, a binary mixture of dolomite and MSW was studied regarding the particle size ratio, in which three different MSW particles sizes (2, 5 and 8 mm) were applied. The effects of superficial gas velocity on mixing were also investigated, whereupon three different inlet velocities were carried (0.15, 0.25 and 0.4 m/s). Lastly, the binary mixture segregation profile was evaluated along the bed height and diameter so to determine the axial and longitudinal solids distribution. Mixing and segregation index values were retrieved to evaluate the quality of the mixture for each case. Indexes were gathered accordingly to the standard deviation approach described in Section 4.7.

The MSW particle size effect on the mixture is shown in Figure 9a. For this analysis, the operating conditions were settled for a superficial gas velocity of 0.25 m/s, simulation time 3 s, and temperature 873 K. Results present two distribution lines for each solid specie (dolomite and MSW) with both

pointing out a clear particle size effect on the fluidization. Besides the size, the particles density also has effect on the mixture, once the dolomite density is placed at 2870 kg/m^3 , and MSW at 247 kg/m^3 (Table 2). The quality of the mixture estimated by the indexes will therefore also comprise the density effect, however, as we merely have two solid species to consider, only the MSW particles sizes were varied in this study. The mixture composed of smaller MSW particles (2 mm) shows a mixing index closer to one ($M = 1$, fully mixed), while the mixture composed of the larger particle presents the lowest mixing index measured. As the smaller MSW particles (2 mm), are the closest in size to the dolomite particles (0.5 mm), the mixing quality is the nearest to achieve a fully mixed state. Opposing, the larger particles (5 and 8 mm), show a gradual mixing index decrease, given to the larger dolomite-MSW particle size ratio, in which the 8 mm case shows the lowest mixing quality by being the most distant from one. Despite following the same trends, the two distribution lines present slightly different mixing indexes for each solid specie in the same mixture, with MSW showing superior mixing in all situations (Figure 9a,b).

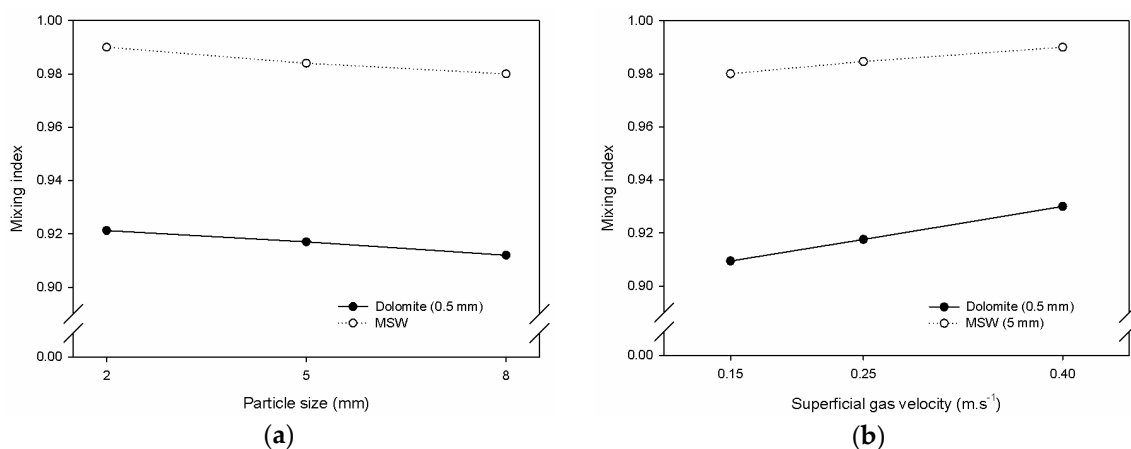


Figure 9. Mixing index study: (a) MSW particle size effect on mixing; (b) superficial gas velocity effect on mixing.

Previous studies found in the literature consider that superficial gas velocity has direct effect over the solids distribution along the bed, mentioning that, the greater the fluidization velocity is, the better the particle mixing will be [38]. The superficial gas velocity effect on the mixing is presented in Figure 9b. Three different superficial velocities were set for this study (0.15, 0.25 and 0.4 m/s), MSW particle size was kept at 5 mm, and operating temperature at 873 K. Results confirm the assumptions found in the literature, higher superficial gas velocity (0.4 m/s) showed better mixing index, while for lower superficial gas velocities (0.15 and 0.25 m/s), mixing index weakens. The operating temperature was also assessed regarding its effect over the mixing and segregation phenomena. For these simulation runs the operating temperature was varied (873, 973 and 1073 K), however, it was found to have very little effect on the gas and solids mixing. Same considerations were drawn by studies reported in the literature [40].

Figure 10a,b shows the solids segregation along the bed height and bed diameter, respectively. Alongside, scaled instantaneous dolomite and MSW volume fraction contours give a perspective of the solids distribution (Figure 10c,d). Instantaneous solids volume fractions meet the same assumptions drawn from the mean volume fraction contours in Section 5.2, with dolomite migrating at the bottom (heavier), and MSW congregating in the top of the bed (lighter). Simulations were conducted at a superficial gas velocity of 0.25 m/s , MSW particle size of 5 mm, and operating temperature 873 K. From a general view at the segregation indexes, one can see that dolomite shows increased segregation compared to MSW. Regarding the segregation effect along the bed height, dolomite shows a progressive segregation rise from bottom to top, meeting its maximum around 0.1 m height. This same maximum coincides with the highest solid concentration (red colored) given by the dolomite volume

fraction contour at 0.1 m height (Figure 10c). As for MSW, segregation is only noticeable at 0.2 m height onwards.

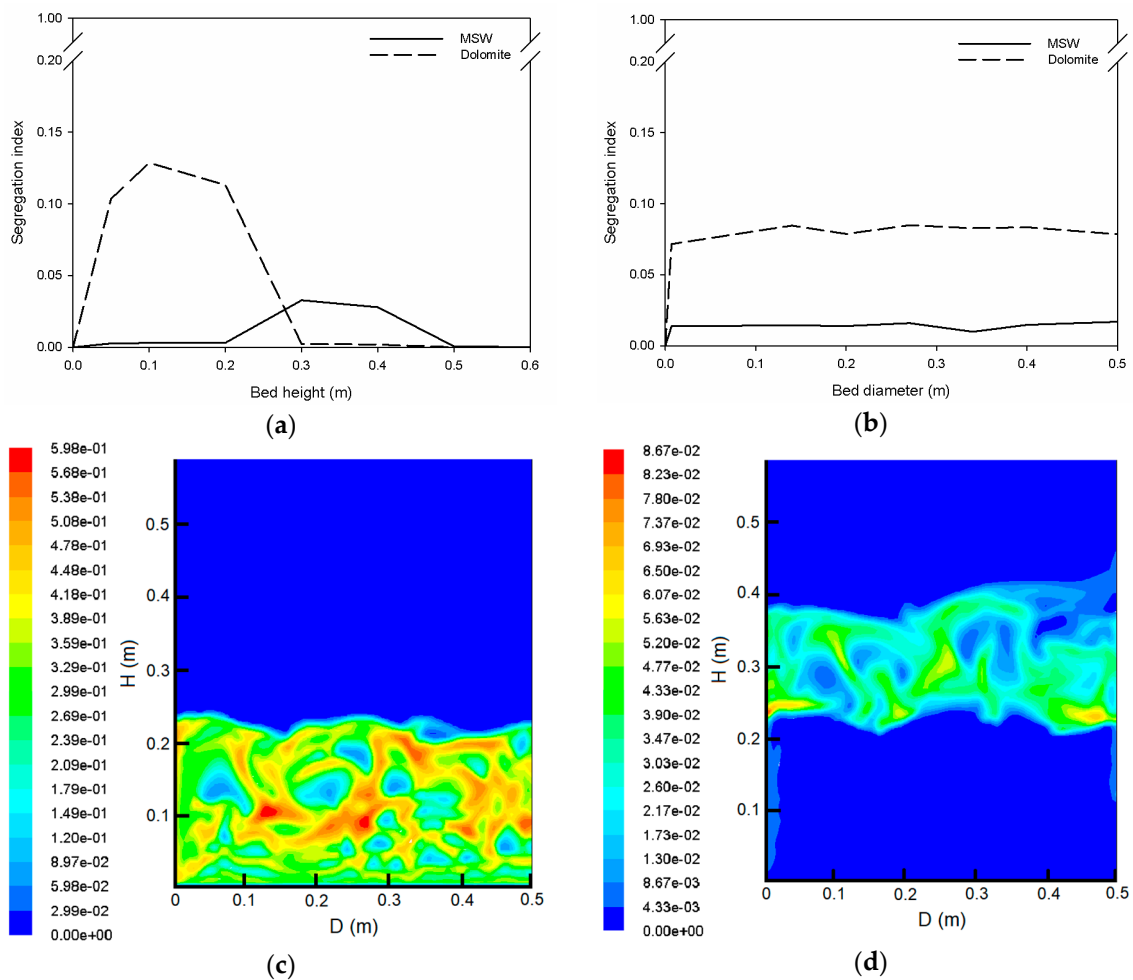


Figure 10. Segregation index distribution: (a) segregation along bed height ($H = 0.6$ m); (b) segregation along the bed diameter ($D = 0.5$ m); (c) dolomite scaled instantaneous volume fraction contour ($t = 3$ s); (d) MSW scaled instantaneous volume fraction contour ($t = 3$ s).

Once more, the 0.3 m height segregation maximum detected for the MSW is consistent with the yellow stains seen in the volume fraction contour (Figure 10d). The spatial arrangement of the segregation indexes along the bed height concur with the solids distribution along the bed, with dolomite presenting segregation merely at the bottom, and MSW at the high near surface region. Regarding the bed diameter direction (Figure 10b), both dolomite and MSW show a more constant profile without noticeable changes. Notwithstanding, on the dolomite profile two small peaks can be distinguished and directly associated with the increased dolomite concentration shown by the volume fraction contour at about 0.15 and 0.25 m width (Figure 10c). Concerning the MSW profile, a subtle segregation decrease between 0.3 and 0.4 m width is consistent with the gas bubble depicted in the volume fraction contour, measuring little solid presence.

As dolomite and MSW have different sizes and densities, the drag force acting on the particles is different, leading particles to gain different velocities within the bed, and so, particle segregation progresses. Overall, the bed showed a naturally good mixing behavior, once the mixing indexes were always very close to one, even for higher particle size ratio mixtures, and the segregation indexes always very close to zero.

5.4. Solid Phases Static Temperature Distribution

As the simulation time progresses the temperature distribution within the fluidized bed constantly develops until a thermal equilibrium is achieved, fluctuating around a constant value. The static temperature contours distribution is presented in Figure 11a for the three-size MSW particles ratio (2, 5 and 8 mm).

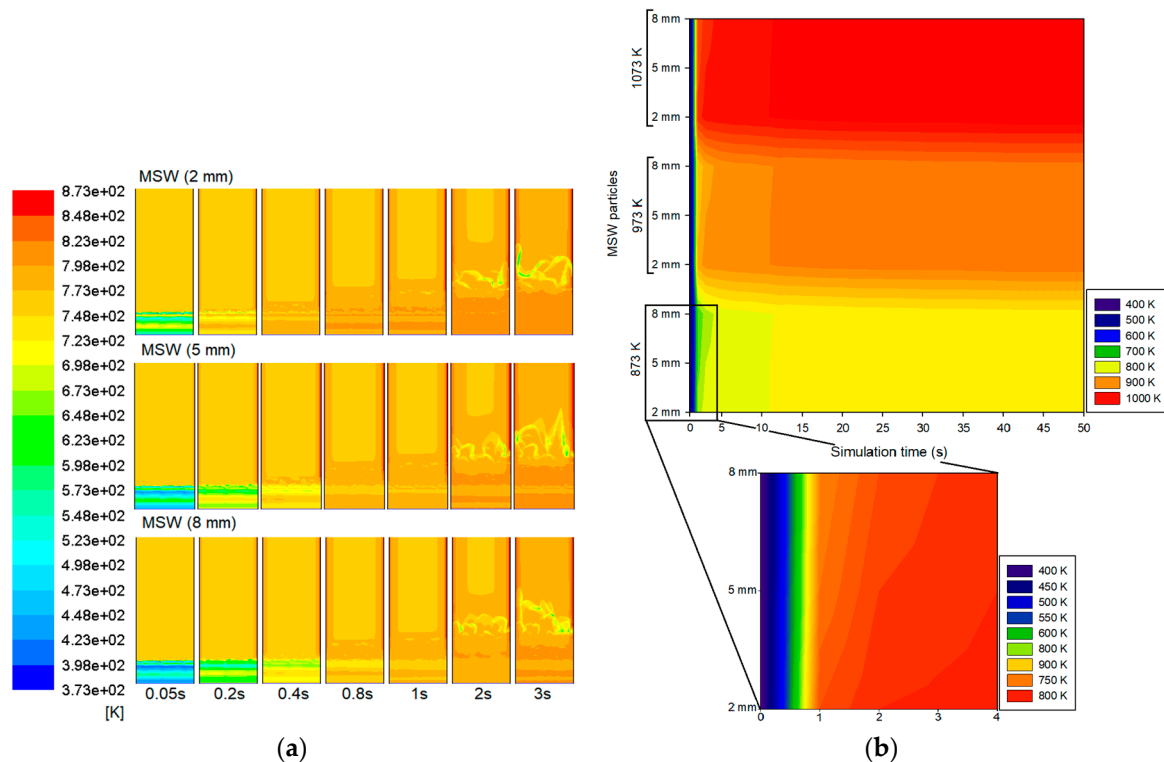


Figure 11. Heat transference performance: (a) static temperature contours of the three MSW particles sizes, during a 3 s simulation time and operating temperature of 873 K; (b) MSW particles static temperature variation at 873, 973 and 1073 K, along the total simulation time of 50 s.

The MSW-dolomite heat transfer performance study was established by setting the following initial temperatures: 373 K for MSW, 823 K for dolomite, 773 K for the air flux, and 873 K for the heated reactor walls. Remaining operating conditions, superficial gas velocity and simulation time were set to 0.25 m/s and 50 s, respectively. The static temperature contours depict the heat transfer dependency on the MSW particles size in the binary mixture. Smaller MSW particles (2 mm) show increased heat transfer when compared with larger MSW particles (5 and 8 mm). This heat transfer inequality is especially prominent at 0.4 s, here the bed region still shows a light green color for 5 and 8 mm MSW particles, while a bright yellow color is seen for 2 mm MSW. Such behavior confirms that, higher the MSW-dolomite mixture size ratio, slower is the temperature increase. The two solids start to reach the thermal equilibrium around the 3 s of simulation time, at this period, identical temperature distribution is found for the three MSW size ratios contours. In the first stages of the fluidization process, the MSW temperature promptly increases as the heat is transferred from the hot dolomite (firstly at 823 K) to MSW particles (firstly at 373 K). In opposition to the MSW particles temperature increase, the dolomite temperature will gradually decrease until the heat transfer between the two species reaches the thermal equilibrium. Yet, the dolomite temperature does not lower significantly from the dolomite-to-MSW heat transference, which is justifiable by the low amount of MSW present in the binary mixture. The temperature increase within the fluidized bed will also be favored throughout the fluidization process by the heated air inflow and the heated reactor walls, shown by the orange red

color in the near wall regions. The static temperature contours presented at 2 and 3 s of simulation time show some small low temperature smudges, which may result from conduction and convection effects from the solid-gas interphase, with the air temperature decreasing due to the solids temperature rise at the bed. In addition, this unevenly distributed heat was found to be due to poor convective heat transfer at the solids-gas interphase [41].

The static temperature variation for the three MSW sizes (2, 5 and 8 mm) at the three operating temperatures tested (873, 973 and 1073 K) is shown along the 50 s simulation time in Figure 11b. Results show that larger MSW particles take more time to increase their temperature within the fluidized bed throughout the fluidization process, as previously seen in the static temperature contours. The zoom in into the first 4 s of simulation time confirms the faster temperature increase for the 2 mm MSW particles, while 8 mm particle shows the slowest increase of the three particles set. This close heat transfer variation is shown for the 873 K alone, once the 973 and 1073 K showed identical distribution rates, but at higher temperatures. Most of the heat transference within the fluidized bed occurs in the first stages of the simulation time, with the MSW requiring around 2 to 3 s to obtain 90% of the final temperature. Such is given to the good mixing behavior and the high heat transference rates attributed to the fluidized beds, allowing the solids to achieve high temperatures very quickly. In this system, it was seen that MSW has about 3 s of residence time, when operated at a superficial gas velocity of 0.25 m/s. Temperature variations between the three MSW size ratios cease after 4 s of simulation time, once the thermal equilibrium is established. The static temperature contours, and the particles heat transfer performance along simulation time go accordingly with previous results found in the literature [38].

6. Conclusions

The hydrodynamics and heat transfer of MSW gasification were studied in a pilot scale fluidized bed reactor by applying a 2-D CFD model. The already previously developed and extensively validated numerical model was reassessed by improving hydrodynamics behavior with more realistic UDFs for drag and heat transfer exchange. Given that the trends were effectively predicted, the applied hydrodynamics sub-model was considered to be sufficiently robust. Solids volume fraction profiles showed that lighter MSW particles migrate to upper bed regions, while heavier dolomite particles were found to accumulate at the bottom of the bed. MSW particles showed superior axial velocity compared to dolomite. Additionally, higher superficial gas velocity led to increased entropy of the solid particles within the fluidized bed. Regarding mixing and segregation phenomena, smaller MSW particles revealed a more uniform mixing, due to its lower size ratio with dolomite. Moreover, better mixing behavior was obtained by increasing the superficial gas velocity. It was found that smaller MSW particles led to enhanced heating rates when compared to larger particles. Finally, syngas runs showed a decrease in the error range when compared to former results obtained without these new hydrodynamic features.

Acknowledgments: We would like to thank Luís Tarelho (University of Aveiro, Portugal) for the kindness in allowing us the experimental fluidization curves for validation purposes. Also, we would like to express our gratitude to the Portuguese Foundation for Science and Technology (FCT) for the project IF/01772/2014.

Author Contributions: J.C. and V.S. carried out CFD simulations and analysis. All authors contributed to writing and reviewing of the manuscript. V.S. supervised the whole work.

Conflicts of Interest: The authors declare no conflict of interest.

References

1. Matteo, U.D.; Nastasi, B.; Albo, A.; Garcia, D.A. Energy contribution of msw (organic fraction of municipal solid waste) to energy-environmental sustainability in urban areas at small scale. *Energies* **2017**, *10*, 229. [[CrossRef](#)]
2. The World Bank. *The World Bank, What a Waste, a Global Review of Solid Waste Management*; The World Bank: Washington, DC, USA, 2012.

3. Shehzad, A.; Bashir, M.J.K.; Sethupathi, S. System analysis for synthesis gas (syngas) production in pakistan from municipal solid waste gasification using a circulating fluidized bed gasifier. *Renew. Sustain. Energy Rev.* **2016**, *60*, 1302–1311. [[CrossRef](#)]
4. BP (British Petroleum). *Statistical Review of World Energy*; BP: London, UK, 2016.
5. Ryu, C.; Shin, D. Combined heat and power from municipal solid waste: Current status and issues in south korea. *Energies* **2013**, *6*, 45–57. [[CrossRef](#)]
6. Volov, Betting on Electric, Moves to Phase Out Conventional Engines. Available online: <https://www.nytimes.com/2017/07/05/business/energy-environment/volvo-hybrid-electric-car.html> (accessed on 2 November 2017).
7. Zhang, D.; Huang, G.; Xu, Y.; Gong, Q. Waste-to-energy in China: Key challenges and opportunities. *Energies* **2015**, *8*, 14182–14196. [[CrossRef](#)]
8. Li, K.; Lee, S.W.; Yuan, G.; Lei, J.; Lin, S.; Weerachanchai, P.; Yang, Y.; Wang, J.-Y. Investigation into the catalytic activity of microporous and mesoporous catalysts in the pyrolysis of waste polyethylene and polypropylene mixture. *Energies* **2016**, *9*, 431. [[CrossRef](#)]
9. Antizar-Ladislao, B.; Turrion-Gomez, J.L. Decentralized energy from waste systems. *Energies* **2010**, *3*, 194–205. [[CrossRef](#)]
10. Al-Hamamre, Z.; Al-Mater, A.; Sweis, F.; Rawajfeh, K. Assessment of the status and outlook of biomass energy in Jordan. *Energy Convers. Manag.* **2014**, *77*, 183–192. [[CrossRef](#)]
11. Lombardi, L.; Carnevale, E.; Corti, A. Analysis of energy recovery potential using innovative technologies of waste gasification. *Waste Manag.* **2012**, *32*, 640–675. [[CrossRef](#)] [[PubMed](#)]
12. Niu, M.; Huang, Y.; Jin, B.; Wang, X. Simulation of syngas production from municipal solid waste gasification in a bubbling fluidized bed using aspen plus. *Ind. Eng. Chem. Res.* **2013**, *52*, 14768–14775. [[CrossRef](#)]
13. Begum, S.; Rasul, M.G.; Akbar, D.; Ramzan, N. Performance analysis of an integrated fixed bed gasifier model for different biomass feedstocks. *Energies* **2013**, *6*, 6508–6524. [[CrossRef](#)]
14. Luo, B.X.S.; Hu, S.L.Z.; Guan, L.C.Y. Influence of particle size on pyrolysis and gasification performance of municipal solid waste in a fixed bed reactor. *Bioresour. Technol.* **2010**, *101*, 6517–6520. [[CrossRef](#)] [[PubMed](#)]
15. Arena, U.; Mastellone, M.L. *Fluidized Bed Pyrolysis of Plastic Wastes*; John Wiley & Sons, Ltd.: Hoboken, NJ, USA, 2006.
16. Couto, N.D.; Silva, V.B.; Rouboa, A. Assessment on steam gasification of municipal solid waste against biomass substrates. *Energy Convers. Manag.* **2016**, *124*, 92–103. [[CrossRef](#)]
17. Silva, V.; Monteiro, E.; Couto, N.; Brito, P.; Rouboa, A. Analysis of syngas quality from Portuguese biomasses: An experimental and numerical study. *Energy Fuels* **2014**, *28*, 5766–5777. [[CrossRef](#)]
18. Silva, V.; Rouboa, A. Using a two-stage equilibrium model to simulate oxygen air enriched gasification of pine biomass residues. *Fuel Process. Technol.* **2013**, *109*, 111–117. [[CrossRef](#)]
19. Couto, N.; Silva, V.; Monteiro, E.; Brito, P.; Rouboa, A. Using an eulerian-granular 2-d multiphase cfd model to simulate oxygen air enriched gasification of agroindustrial residues. *Renew. Energy* **2015**, *77*, 174–181. [[CrossRef](#)]
20. Couto, N.; Silva, V.; Monteiro, E.; Teixeira, S.; Chacartegui, R.; Bouziane, K.; Brito, P.S.D.; Rouboa, A. Numerical and experimental analysis of municipal solid wastes gasification process. *Appl. Therm. Eng.* **2015**, *78*, 185–195. [[CrossRef](#)]
21. Couto, N.; Silva, V.; Rouboa, A. Municipal solid waste gasification in semi-industrial conditions using air-CO₂ mixtures. *Energy* **2016**, *104*, 42–52. [[CrossRef](#)]
22. European Environment Agency. *Municipal Waste Management, Portugal*; European Environment Agency: København, Denmark, 2016.
23. Statistics Portugal. *Waste Statistics*; Statistics Portugal: Lisboa, Portugal, 2014.
24. Eurostat. Municipal Waste Statistics. Available online: http://ec.europa.eu/eurostat/statistics-explained/index.php/Municipal_waste_statistics (accessed on 8 August 2017).
25. APA (American Psychological Association). Data on Urban Waste. Available online: <https://www.apambiente.pt/index.php?ref=16&subref=84&sub2ref=933&sub3ref=936> (accessed on 8 August 2017).
26. APA (American Psychological Association). *Urban Residues Annual Report*; Portuguese Environmental Agency: Amadora, Portugal, 2015.
27. GSTC (Global Sustainable Tourism Council). *Waste to Energy Gasification*. Available online: <http://www.gasification-syngas.org> (accessed on 29 August 2017).

28. Panepinto, D.; Tedesco, V.; Brizio, E.; Genon, G. Environmental performances and energy efficiency for msw gasification treatment. *Waste Biomass Valoriz.* **2015**, *6*, 123–135. [[CrossRef](#)]
29. REA (Renewable Energy Association). *Gasification and Pyrolysis*; Renewable Energy Association: London, UK, 2013.
30. Afrooz, I.; Sinnathambi, C.; Karuppanan, S.; Ching, D. Cfd simulation of bubbling fluidized bed: Effect of distributor plate orifice pattern configuration on hydrodynamics of gas-solid mixing. *ARPN J. Eng. Appl. Sci.* **2006**, *11*, 11954–11959.
31. Sharma, A.; Wang, S.; Pareek, V.; Yang, H.; Zhang, D. Cfd modeling of mixing/segregation behavior of biomass and biochar particles in a bubbling fluidized bed. *Chem. Eng. Sci.* **2014**, *106*, 264–274. [[CrossRef](#)]
32. Manna, L.; Zanetti, M.C.; Genon, G. Modeling biogas production at landfill site. *Resour. Conserv. Recycl.* **1996**, *26*, 1–14. [[CrossRef](#)]
33. Couto, N.; Silva, V.; Monteiro, E.; Rouboa, A. Exergy analysis of portuguese municipal solid waste treatment via steam gasification. *Energy Convers. Manag.* **2017**, *134*, 235–246. [[CrossRef](#)]
34. Syamlal, M.; Rogers, T.J. *Mfix Documentation: Vol. 1. Theory Guide*; National Technical Information Service: Springfield, VA, USA, 1993.
35. Lun, C.; Savage, S.B.; Jeffrey, D.; Chepuriniy, N. Kinetic theories for granular flow: Inelastic particles in couette flow and slightly inelastic particles in a general flow field. *J. Fluid Mech.* **1984**, *140*, 223–256. [[CrossRef](#)]
36. Peng, Z.; Doroodchi, E.; Alghamdi, Y.; Moghtaderi, B. Mixing and segregation of solid mixtures in bubbling fluidized beds under conditions pertinent to the fuel reactor of a chemical looping system. *Powder Technol.* **2013**, *235*, 823–837. [[CrossRef](#)]
37. Vepsalainen, A.; Shah, S.; Ritvanen, J.; Hyppanen, T. Bed sherwood number in fluidised bed combustion by eulerian cfd modelling. *Chem. Eng. Sci.* **2013**, *93*, 206–213. [[CrossRef](#)]
38. Dinh, C.; Liao, C.; Hsiao, S. Numerical study of hydrodynamics with surface heat transfer in a bubbling fluidized-bed reactor applied to fast pyrolysis of rice husk. *Adv. Powder Technol.* **2017**, *28*, 419–429. [[CrossRef](#)]
39. Huilin, L.; Yurong, H.; Gidaspow, D.; Lidan, Y.; Yukun, Q. Size segregation of binary mixture of solids in bubbling fluidized beds. *Powder Technol.* **2003**, *134*, 86–97. [[CrossRef](#)]
40. Du, B.; Fan, L.-S.; Wei, F.; Warsito, W. Gas and solids mixing in a turbulent fluidized bed. *Part. Technol. Fluid. AIChE J.* **2002**, *48*, 1896–1909. [[CrossRef](#)]
41. Ngoh, J.; Lim, E.W.C. Effects of particle size and bubbling behavior on heat transfer in gas fluidized beds. *Appl. Therm. Eng.* **2016**, *105*, 225–242. [[CrossRef](#)]



© 2017 by the authors. Licensee MDPI, Basel, Switzerland. This article is an open access article distributed under the terms and conditions of the Creative Commons Attribution (CC BY) license (<http://creativecommons.org/licenses/by/4.0/>).